Journal of Marine Science and Technology

Volume 26 | Issue 5 Article 10

# QUALITATIVE SURVEY OF A COASTAL REGION FROM A POLARIMETRIC ANALYSIS OF SYNTHETIC APERTURE RADAR IMAGES

Hsiu-Wen Wang
*Department of Graduate Institute of Space Science, National Central University, Taoyuan City, Taiwan, R.O.C.*,
976403004@cc.ncu.edu.tw

Hsuan Ren
*Department of Graduate Institute of Space Science, National Central University, Taoyuan City, Taiwan, R.O.C.*,
hren@csrsr.ncu.edu.tw



## Recommended Citation

Wang, Hsiu-Wen and Ren, Hsuan (2018) "QUALITATIVE SURVEY OF A COASTAL REGION FROM A POLARIMETRIC ANALYSIS OF SYNTHETIC APERTURE RADAR IMAGES," *Journal of Marine Science and Technology*: Vol. 26: Iss. 5, Article 10.
DOI: 10.6119/JMST.201810_26(5).0010
Available at: https://jmstt.ntou.edu.tw/journal/vol26/iss5/10

Journal of Marine Science and Technology, Vol. 26, No. 5, pp. 712-720 (2018)
DOI: 10.6119/JMST.201810_26(5).0010

# QUALITATIVE SURVEY OF A COASTAL REGION FROM A POLARIMETRIC ANALYSIS OF SYNTHETIC APERTURE RADAR IMAGES

Hsiu-Wen Wang and Hsuan Ren

Key words: fully polarimetric SAR images, target decomposition, sandbank change.

## ABSTRACT

This study applied a time series of fully polarimetric synthetic aperture radar (SAR) images using RADARSAT-2 to analyze the polarimetric responses of the west coast of Taiwan. A total of seven images were acquired from 2009 and 2012, covering the low, high, and similar tide levels. A four-component target decomposition algorithm was used to investigate the tidal effects and dynamic ocean interactions of sandbanks near the coast. The experimental results showed that the Yamaguchi four-component decomposition can extract different features in the coastal area efficiently and effectively. From the target decomposition image constructed using the Yamaguchi four-component model, strong double-bounce scattering and weak volume scattering were favorable indicators of oyster farms, whether they were densely arranged or rugged, and surface scattering delineated the water boundaries of sandbanks. Using the extracted water boundaries and tidal-level information from different times, a sandbank elevation model was estimated. The experimental results also revealed that a small offshore sandbank had a displacement of approximately 1.5 km under a tidal level of -1.14 m. Furthermore, large sandbanks had a counterclockwise displacement on the west coast and moved eastward on the eastern coast.

## I. INTRODUCTION

In recent years, environmental monitoring has relied on satellites to achieve observational efficiency and combine multiremote sensing images effectively. A synthetic aperture radar (SAR) is a useful tool for identifying changes in land and ocean environments because its backscattering is sensitive to surface roughness. Holt (2004) stated that radar return is a complex interaction of the transmitted signal, whose characteristics are determined by the radar frequency, polarization, viewing geometry, and illuminated surface. The surface attributes include roughness characteristics, electrical properties, and material composition. Numerous studies have focused on observation of oceanic phenomena using SAR (Thompson, 2004; Vachon et al., 2004), including internal waves (Apel, 2004), underwater bottom topography (Shuchman et al., 1985; Calkoen et al., 1998; Niedermeier et al., 2005; Kim et al., 2016; Zhang et al., 2017), the tidal flat environment using a multifrequency SAR (Ryu et al., 2014, Kim et al., 2016), and surface roughness using the backscattering model (Tanck et al., 1999; Daphne van der Wal et al., 2005) and frequency (Kim et al., 2007; Gade et al., 2008; Park et al., 2009; Choe et al., 2012). Studies using polarization SAR have been conducted for conifer and broadleaf forest classifications using L-band PolSAR (Lee, 2005) and ship detection using a hybrid polarimetric mode involving the L- and C-bands (Gao et al., 2018). Polarimetric SAR has numerous applications in inshore and ground environments through surface backscattering.

The west coast of Taiwan is mainly flat terrain with a sedimentary structure composed of sand and mud. The bathymetry of the mid west coast compared with that of the northern and southern regions is relatively shallow. Considerable variations exist between tidal flow and flow due to surface undulation of the bottom topography. Sandbanks in the west coast can be used to measure costal dynamics, and this observation is crucial for monitoring the ecosystem and natural resources of Taiwan's marine environment. According to SAR images of the ocean surface, is present to the vertical polarization returns is evident separated than horizontal polarization by 5 GHz at the steepest angle of incident at 30 degree (Holt, 2004). In this study, fully polarimetric SAR images from Radarstat-2 from 2009 to 2012 were acquired to examine the costal dynamics of Taiwan's west coast and understand the physical mechanism and structure of sandbanks and oyster farms.

In addition to enabling target decomposition, Lee et al. (2006) confirmed that polarimetric SAR data are useful for selecting areas dominated by double-bounce scattering in oyster farms in L-band AIRSAR images. Choe et al. (2012) revealed that volume scattering and strong depolarization occur on the rough surface of oyster reefs, and that the radar wavelength

*Paper submitted 05/04/18; revised 07/05/18; accepted 09/14/18.* *Author for correspondence: Hsiu-Wen Wang (e-mail: 976403004@cc.ncu.edu.tw) and Hsuan Ren (e-mail: hren@csrsr.ncu.edu.tw).*
*Department of Graduate Institute of Space Science, National Central University, Taoyuan City, Taiwan, R.O.C.*

and multifrequency data of C- and L-band polarimetric SAR systems can be used to detect the naturally distributed oyster reefs in tidal flats. Use of the C-band wavelength is more sensitive and has been noted to result in increased multiple scattering and depolarization effects (Choe et al., 2012).Yamaguchi's four components, namely surface, double-bound, volume, and helix scattering, have been presented in mode-based decomposition studies. A conventional three-component scattering model has been successfully applied to decompose scattering mechanisms under the reflection symmetry condition, but this approach is not suitable for urban area scattering. Therefore, helix scattering power is proposed as the fourth component term for application in the nonreflection symmetry condition (Yamaguchi, 2006). Furthermore, Yamaguchi (2011) revealed that the original coherency matrix is transformed through rotation, and urban areas are recognized as double-bounce objects from volume scattering. The Yamaguchi method has been applied to land cover classification (Sun et al., 2015; Brown et al., 2016; Varghese, 2016) and building mapping (Hong and Wdowinski, 2012; Zhai and Huang, 2016) for environment observations that utilize observed scattering mechanisms in polarimetric SAR data. Additionally, Varghes et al. (2015) compared six decompositions in forest density, and the results showed that the Yamaguchi four-component (Y4R) decomposition provided superior classification results compared with other methods. Continuing from the aforementioned works, the present study applied target decomposition to identify the surface features of oyster farms and sandbanks in Taiwan's west coastal region alongside changes in both over a 3-year period using a time series of fully polarimetric SAR images obtained from RADARSAT-2.

## II. POLARIMETRIC TARGET DECOMPOSITION

In real-world scenarios, coastal regions usually contain numerous objects, such as the sea surface, oyster farms, and sandbanks. The use of scattering to identify physical structures has been intensively researched, with Pauli decomposition widely applied for this approach. This decomposition expresses the scattering matrix $S$ as the complex sum of the Pauli matrices, where an elementary scattering mechanism is associated with each basis matrix, expressed as

$$S=\begin{bmatrix} S_{HH} & S_{HV} \\ S_{VH} & S_{VV} \end{bmatrix}=\frac{a}{\sqrt{2}}\begin{bmatrix} 1 & 0 \\ 0 & 1 \end{bmatrix}+\frac{b}{\sqrt{2}}\begin{bmatrix} 1 & 0 \\ 0 & -1 \end{bmatrix}+\frac{c}{\sqrt{2}}\begin{bmatrix} 0 & 1 \\ 1 & 0 \end{bmatrix}+\frac{d}{\sqrt{2}}\begin{bmatrix} 0 & -j \\ j & 0 \end{bmatrix} \quad (1)$$

where $a$, $b$, $c$, and $d$ are complex values and given by

$$a=\frac{S_{HH}+S_{VV}}{\sqrt{2}},\ b=\frac{S_{HH}-S_{VV}}{\sqrt{2}},\ c=\frac{S_{HV}+S_{VH}}{\sqrt{2}},\ d=j\frac{S_{VH}-S_{HV}}{\sqrt{2}} \quad (2)$$

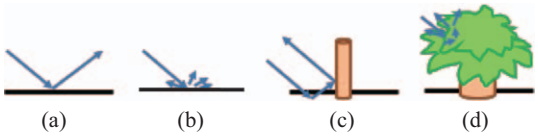


**Fig. 1. Scattering structures: (a) smooth surface, (b) rough surface, (c) double bounce, and (d) volume scattering.**

The coherent composition of the first three scattering mechanisms is illustrated in Fig. 1. Figs. 1(a) and 1(b) show the single scattering from a plane surface (single or odd-bounce scattering), whereas Figs. 1(c) and 1(d) represents the dipole scattering (double-bounce scattering) and volume scattering, respectively. The final components are the antisymmetric components of the scattering matrix $S$. In the monostatic case, where $S_{HV} = S_{VH}$, the Pauli matrix basis can be reduced to the first three matrices because $d = 0$, and the Pauli vector is defined as

$$k_p=\frac{1}{\sqrt{2}}\begin{bmatrix} S_{HH}+S_{VV} \\ S_{HH}-S_{VV} \\ 2S_{HV} \end{bmatrix} \quad (3)$$

This coherent target decomposition is useful if only one target component is dominant (e.g., dihedral or trihedral edge contributions in urban areas or as calibration targets), and the other components are only provided to support the construction of a suitable basis for the whole space of targets (Freeman and Durden, 1998). In the Y4R model (Yamaguchi et al., 2005), to resolve problems caused by an urban landscape such as rotation of the coherency matrix, physical scattering models are enhanced from surface and double-bounce scattering to minimize the cross-polarized HV component, also known as desying (Yamaguchi et al., 2005 ) or deorientation (Lee and Pottier, 2009). Double-bounce scattering is unable to easily recognize objects in urban areas because volume scattering is dominant in such areas with a mixture of tall and regularly sized buildings.

The coherency matrix is expressed as follows:

$$\langle[T]\rangle^{HV}=\langle k_p k_p^{*T}\rangle \quad (4)$$

$$\langle[T]\rangle^{HV}=\begin{bmatrix} \frac{1}{2}\langle|S_{HH}+S_{VV}|^2\rangle & \frac{1}{2}\langle(S_{HH}+S_{VV})(S_{HH}-S_{VV})^*\rangle & \langle(S_{HH}+S_{VV})S_{HV}^*\rangle \\ \frac{1}{2}\langle(S_{HH}-S_{VV})(S_{HH}+S_{VV})^*\rangle & \frac{1}{2}\langle|S_{HH}-S_{VV}|^2\rangle & \langle(S_{HH}-S_{VV})S_{HV}^*\rangle \\ \langle S_{HV}(S_{HH}+S_{VV})^*\rangle & \langle S_{HV}(S_{HH}-S_{VV})^*\rangle & \langle 2|S_{HV}|^2\rangle \end{bmatrix} \quad (5)$$

From Yamaguchi et al. (2006), the coherency matrix (5) can be expanded as

$$\begin{aligned}\langle[T]\rangle^{HV} &= f_s\langle[T]\rangle^{hv}_{surface} + f_d\langle[T]\rangle^{hv}_{double} + f_v\langle[T]\rangle^{hv}_{volume} + f_c\langle[T]\rangle^{hv}_{helix} \\ &= f_s\begin{bmatrix}1 & \beta^* & 0\\ \beta & |\beta|^2 & 0\\ 0 & 0 & 0\end{bmatrix} + f_d\begin{bmatrix}|\alpha|^2 & \alpha & 0\\ \alpha^* & 1 & 0\\ 0 & 0 & 0\end{bmatrix} + \frac{f_v}{4}\begin{bmatrix}2 & 0 & 0\\ 0 & 1 & 0\\ 0 & 0 & 1\end{bmatrix} + \frac{f_c}{2}\begin{bmatrix}0 & 0 & 0\\ 0 & 1 & \pm j\\ 0 & \mp j & 1\end{bmatrix}\end{aligned} \quad (6)$$

where $f_s$, $f_d$, $f_v$, and $f_c$ are the expansion coefficients to be determined from polarimetric data. $\alpha$ and $\beta$ are defined as $\alpha = (S_{HH} + S_{VV})/(S_{HH} - S_{VV})$ and $\beta = (R_H - R_V)/(R_H + R_V)$, where $R_H$ and $R_V$ are the function of incident angle and relative dielectric constant. $|\alpha| < 1$ corresponds to the contribution of the double-bounce scattering, and $|\beta| < 1$ corresponds to the contribution of the surface scattering. The window size for image processing in this study was 5 × 5, which was used to estimate the coherency matrix.

Lee et al. (2011) stated that the polarization orientation angle is the angle of rotation around the line of sight. When symmetrical media are reflected, such as a horizontal surface, the orientation angle is zero. To reduce the power of volume scattering and increase the power of double-bounce scattering, the polarization orientation angle is induced by surfaces with nonzero azimuth slopes. This can be achieved by multiplying the unitary rotation matrix by the $R_n[\theta]$ rotation matrix without loss of generality (Yamaguchi et al., 2011). Assuming that the measured coherency matrix is

$$\left[T(\theta)\right] = \begin{bmatrix}T_{11}(\theta) & T_{12}(\theta) & T_{13}(\theta)\\ T_{21}(\theta) & T_{22}(\theta) & T_{23}(\theta)\\ T_{31}(\theta) & T_{32}(\theta) & T_{33}(\theta)\end{bmatrix} \quad (7)$$

then the coherency matrix after the rotation matrix can be obtained by

$$\left[T(\theta)\right] = \left[R_p(\theta)\right][T]\left[R_p(\theta)\right]^{*T} \quad (8)$$

$$\left[R_p(\theta)\right] = \begin{bmatrix}1 & 0 & 0\\ 0 & \cos 2\theta & \sin 2\theta\\ 0 & -\sin 2\theta & \cos 2\theta\end{bmatrix} \quad (9)$$

According to the decomposition algorithm, the total scattered power,

$$P_t = P_s + P_d + P_v + P_c = \left\langle |S_{HH}|^2 + 2|S_{HV}|^2 + |S_{VV}|^2 \right\rangle \quad (10)$$

can be decomposed into four scattering components $P_s$, $P_d$, $P_v$, and $P_c$, corresponding to surface, double-bounce, volume, and helix scattering, respectively, which are determined by the expansion coefficient given in (6):

$$P_s = f_s(1+|\beta|^2),\ P_d = f_d(1+|\alpha|^2),\ P_v = f_v,\ P_c = f_c. \quad (11)$$

Before decomposition, orientation compensation was applied to correct the azimuthal angle effect on double-bounce scattering. For example, a human-made building that is not aligned with the along-track direction should be compensated for by using azimuthal variations (Yamaguchi et al., 2006; Lee and Pottier, 2009).

Due to the unknown scattering mechanisms in offshore regions, this parameterization of a dominant average scattering mechanism can extract crucial target information on certain forms of direct random media scattering; hence, eigenvector decomposition was proposed by Cloude and Pottier.

$$<[T]>=[U_3][\Sigma][U_3]^{-1} \quad (12)$$

where $[\Sigma]$ is a 3 × 3 diagonal matrix with nonnegative real elements, and $[U_3]$ is a unitary matrix of the three-unit orthogonal eigenvectors.

$$\begin{aligned}\left[U_3\right] &= \left[u_1 \quad u_2 \quad u_3\right] \\ &= \begin{bmatrix}\cos\alpha_1 & \cos\alpha_2 & \cos\alpha_3\\ \sin\alpha_1\cos\beta_1 e^{j\delta_1} & \sin\alpha_2\cos\beta_2 e^{j\delta_2} & \sin\alpha_3\cos\beta_3 e^{j\delta_3}\\ \sin\alpha_1\sin\beta_1 e^{j\gamma_3} & \sin\alpha_2\sin\beta_2 e^{j\gamma_3} & \sin\alpha_3\sin\beta_3 e^{j\gamma_3}\end{bmatrix}\end{aligned} \quad (13)$$

Parameter $\alpha$ is an indicator of the type of scattering mechanism, and parameter $\beta$ is the physical orientation of an object around the line of sight; $\delta$ and $\gamma$ indicate the phase relationship of the signals. The dominant scattering mechanism for each pixel is measured using

$$\bar{\alpha} = \sum_{i=1}^{n} P_i\alpha_i,\ 0 \le \bar{\alpha} \le 90 \quad (14)$$

This direction information represents surface scattering, double-bounce scattering, and volume scattering at 0-42.5, 42.5-47.5, and 47.5-90, respectively (Cloude and Pottier, 1997).

The entropy is calculated by the probability contribution of each $\lambda_i$ as

$$\begin{aligned}P_i &= \frac{\lambda_i}{\sum_{j=1}^{n}\lambda_j} \\ H &= \sum_{i=1}^{n} -P_i\log_n P_i,\ 0 \le H \le 1\end{aligned} \quad (15)$$

where $n = 3$ for three scattering mechanism. The entropy is a measurement of the randomness of the scattering mechanisms. $H = 0$ indicates the domination of a single scattering mechanism while $H = 1$ indicates a random mixture of all scattering types.

**Table 1. Tide and wind data at acquisition time of RADARSAT-2 images.**

| Item | Data | Tide (m) | Wind direction | Wind speed (m/s) |
|---|---|---|---|---|
| 1 | 2009/3/15 | -1.14 | NNE | 8.3 |
| 2 | 2009/4/08 | -0.71 | NNE | 12.6 |
| 3 | 2009/5/26 | -1.71 | NNE | 7.9 |
| 4 | 2009/6/19 | 0.90 | WSW | 3.3 |
| 5 | 2009/8/06 | -1.12 | NNE | 6.7 |
| 6 | 2009/8/30 | 0.91 | NNE | 8.3 |
| 7 | 2012/6/03 | -0.72 | N | 12.4 |

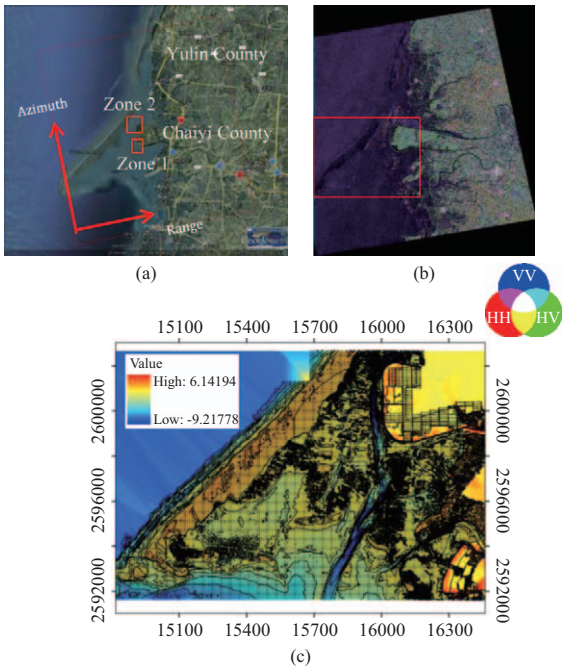


**Fig. 2. (a) Optical image from Google Earth of the study site. (b) False color composite of SAR images where the red frame indicates the study area of 25 × 50 km$^2$. (c) Bathymetry measurement using sonar in 2006.**

## III. STUDY SITE AND MATERIAL

The west coast of Taiwan is mainly flat terrain with a sedimentary structure composed of sand and mud. The bathymetry of the mid west coastal region is relatively shallow compared with that of the northern and southern coastal regions. The intertidal level exhibits substantial variations due to surface undulation of the bottom topography. The study area covered the coastal regions of Yunlin County and Chiayi County, for which the off-coast sandbanks and oyster fields are presented in Fig. 2(a). The study site is indicated in a red rectangle in Fig. 2(b), and represents an area of 25 × 50 km$^2$. A total of seven images were acquired from along the Chiayi coastal area from 2009 and 2012 using the RADARSAT-2 in fully polarimetric mode (HH, HV, VH, and VV). These observational data sets were collected at ascending orbits at an incidence angle of 34.4°-36°.

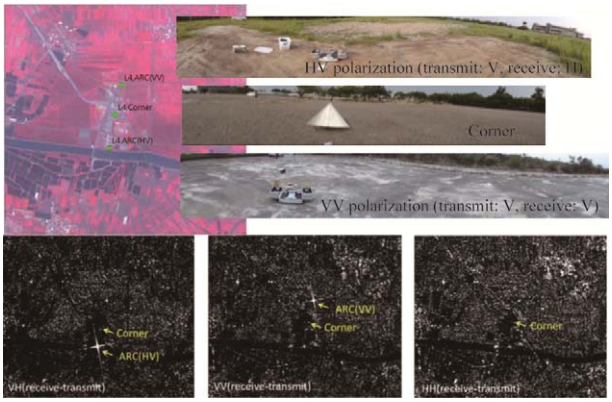


**Fig. 3. In situ ground survey sites of RADARSAT-2.**

Fig. 2(b) displays a false color composite of one image, where HH, HV, and VV components are shown in red, green, and blue, respectively. The bathymetry around the littoral zones measured through sonar at 50 m of spatial resolution (presented in Fig. 2(c)) was used for image analysis. Kim et al. (2016) revealed that the ocean waveheight spectrum was perturbed by varying surface currents under windy conditions at the time of SAR data acquisition. Table 1 shows that synchronous collection of the tide, wind speed, and wind direction corresponded to image acquisition time, which can be used to determine the status of the intertidal zone environment.

## IV. EXPERIMENT RESULTS AND DISCUSSION

Active radar calibrators (ARCs) can be used to derive both the amplitude and phase characteristics of a multichannel polarimetric SAR from complex image data (Freeman et al., 1990). In this study, an experiment for the validation of target decomposition was conducted using RADARSAT-2.

The trihedral corner reflector (Fig. 3) is the most practical device for calibrating radar systems. It also has a wide beamwidth (approximately 30°) in both azimuth and elevation dimensions and can be used to calibrate radar systems with different frequencies. The peak values for the radar cross section for an ideal trihedral corner and its polarization signature are

$$RCS = \frac{4\pi a^4}{3\lambda^2}, \; S_{tri} = \begin{bmatrix} 1 & 0 \\ 0 & 1 \end{bmatrix} \tag{12}$$

where $a$ is the leg length of the trihedral corner (Freeman et al., 1990). The VV ARC achieves vertical polarization on both transmission and receiving ends, where the polarization of defining characteristics is typical of single-bounce and double-bounce scattering. The HV ARC receives horizontal polarization and transmits vertical polarization, and this cross-polarization can determine the physical characteristics of volume scattering.

The target detection features of trihedral corner reflectors and ARCs can be obtained from the Y4R decompositions on the target

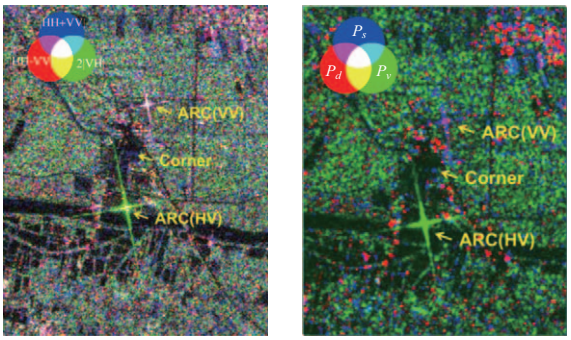


(a) (b)

**Fig. 4. (a) Pauli of 2012/6/3 and (b) Y4R of 2012/6/3.**

coherency matrix *T*. In Fig. 4, the Y4R is employed to consider the azimuth slope between the SAR observation plane and surface roughness plane. As presented in Fig. 4(a), the VV ARC exhibits single-bounce and volume scattering. The Y4R decomposition includes rotation angle; therefore in Fig. 4(b), the overall power of VV ARC compared with the rotated double-bounce polarization power was significantly improved with a reduction in volume power.

To understand the characteristics of polarimetric backscattering in order to detect target features in this coastal region, in situ ground surveys were conducted to identify the sandbanks, oyster farms, and sea surfaces of the study site. In Fig. 2(a), zone 1 was used to identify the double-bounce scattering from oyster farms with racks only, whereas zone 2 was employed to characterize the surface and volume scattering from both sandbanks and oyster farms.

## 1. Oyster Farms

The oyster farms were diamond- and curve-shaped near zone 1, and they were submerged at high tide and exposed at low tide. False color composite images of the three components are shown in Figs. 5(b) and 5(c). In Fig. 5(b), the average DN values for oyster farms within the white frame with double-bounce, volume, and surface scattering are 0.3903, 0.1051, and 0.2822, respectively. At the same area in Fig. 5(c), the average DN values with double-bounce, volume, and surface scattering are 0.1392, 0.011, and 0.0062, respectively. The results presented in Fig. 5(d) show that the dipole of double-bounce scattering was dominated by a single curve-shaped feature type on the coastal region, which could be clearly observed at a tidal level of -0.71 m. In Figs. 6(b) and 6(c), oyster farms in zone 2 can be clearly observed from the RADARSAT-2 SAR images: the double-bounce and volume scattering of oyster farms were directly identified using Pauli and Y4R decompositions, and the domination of double-bounce and volume scattering varied asynchronously at different tidal levels and for different oyster farm layouts.

## 2. Sandbanks

The submerged and exposed images of sandbanks also depended on tidal levels. Fig. 6(a) shows a photograph of oyster

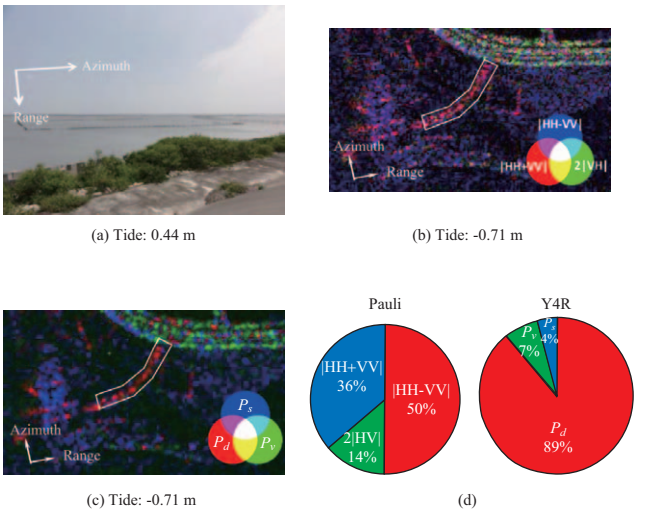


(a) Tide: 0.44 m (b) Tide: -0.71 m

(c) Tide: -0.71 m (d)

**Fig. 5. (a) Photographs of oyster farms taken on June 3, 2012; (b) Pauli-based image; (c) Y4R image; and (d) the proportion within region of interest of the three components from the Pauli and Y4R decompositions.**

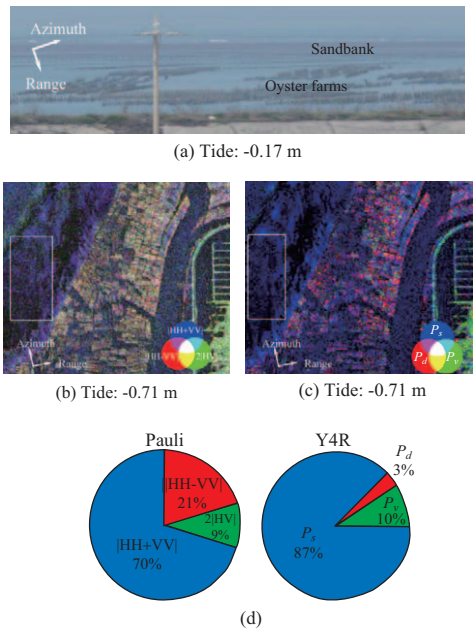


(a) Tide: -0.17 m

(b) Tide: -0.71 m (c) Tide: -0.71 m

(d)

**Fig. 6. (a) Photograph of oyster farms and a sandbank taken on June 3,, 2012; (b) Pauli-based image; (c) Y4R image; and (d) the proportion within region of interest of the three components from the Pauli and Y4R decompositions**

farms and a sandbank taken on June 3, 2012. The radar range and azimuth directions are indicated in the photograph. Both Pauli and Y4R color composite images are displayed in Figs. 6(b) and 6(c), respectively. In Fig. 6(b), the average DN values for sandbanks within the white frame with double-bounce, volume, and surface scattering are 0.0974, 0.0442, and 0.3352, respectively. For the same area in Fig. 6(c), average DN values with double-bounce, volume, and surface scattering are 0.0008,

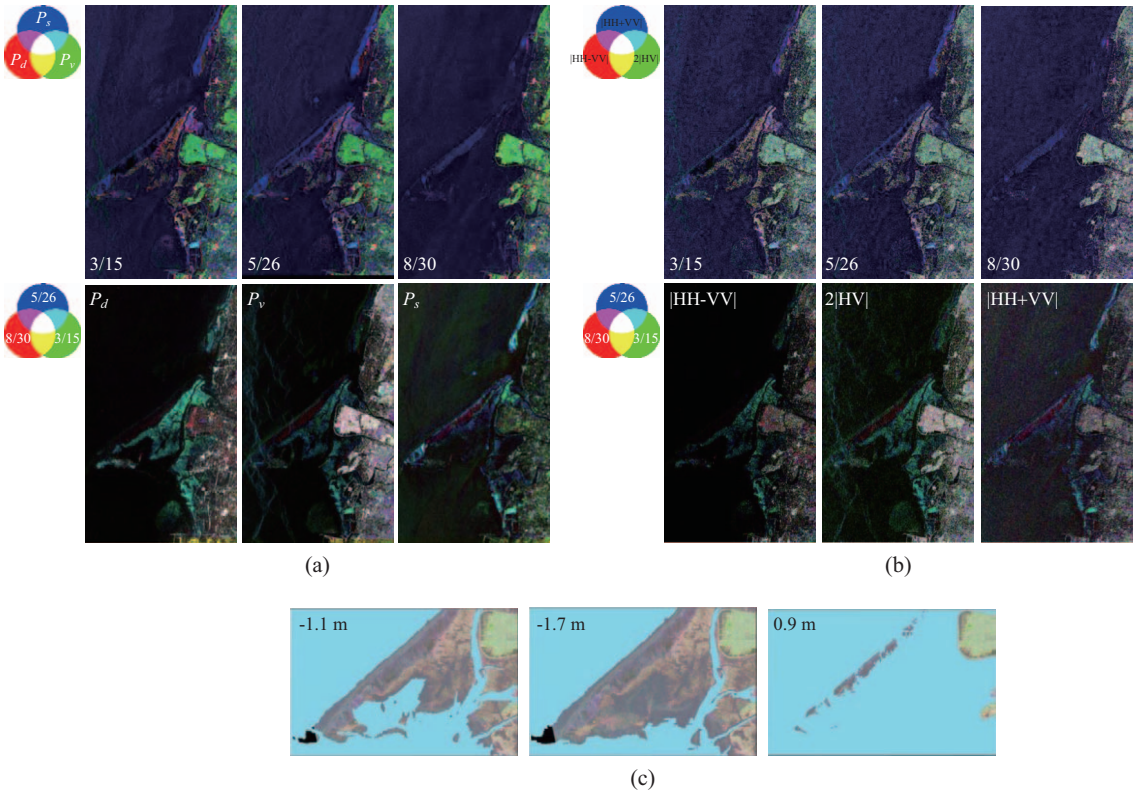


**Fig. 7. (a) Time series of Y4R images on March 15, 2009, May 26, 2009, and August 30, 2009, and multitemporal color composite images; (b) time series of Pauli-based images on March 15, 2009, May 26, 2009, and August 30, 2009, and multitemporal color composite image; and (c) scenarios of the surface topography at different tidal levels on (from left to right) March 15, 2009, May 26, 2009, and August 30, 2009.**

0.0025, and 0.0224, respectively. In Fig. 6(d), $P_s$ from Y4R for the sandbank present considerable surface scattering phenomenon compared with the surface scattering component of the Pauli method. Surface scattering was the dominant type for the sandbank.

## 3. Sandbank Elevation with Different Tidal Levels

Images from three different dates (2009/3/15, 2009/5/26, and 2009/8/30) were selected for analysis. The color composite multitemporal images of Y4R and Pauli decompositions are displayed in Figs. 7(a) and 7(b). The simulations of the surface topography at different tidal levels are shown in Fig. 7(c). Because of low tides, double-bounce scattering from oyster farms was evident on March 15, 2009 and May 26, 2009. At high tide on August 30, 2009, volume and double-bounce scattering were not noted. In all three images, surface scattering from the sandbanks was clearly observed. Double-bounce scattering was dominant over volume scattering on March 15, 2009 along the coastal region, which may have been cause by the sandbanks as they emerged from the sea surface. A comparison between a Pauli-based image (Fig. 7(b)) and Y4R decomposition image (Fig. 7(a)) indicates that Y4R decomposition offers more information about scattering mechanisms and hence the surface features. The results of the Y4R decomposition also show obvious surface and volume scattering characteristics above the large sandbank at low tide. Fig. 7(a) shows that between the large offshore sandbank and the middle sandbank inshore, a small area of surface scattering was noted during low tide on May 26, 2009; notably, at this time Y4R revealed the most significant $P_s$ properties. However, at the same location on March 15, 2009 at low tide (-1.14 m), surface scattering properties were observed, revealing that the surface scattering component was surrounded by the volume scattering component. Radar backscattering from the sea surface over the bottom topography through SAR has been reported, and the method of moments is due to the varying surface current that perturbs small ocean waves; the SAR detects the microwaves backscattered from the perturbed ocean waves with varying levels of surface roughness (Shuchman et al., 1985; Calkoen et al., 1998; Kim et al., 2016). As a result, comparing the Y4R with alpha and entropy target decompositions can enable physical interpretations of statistical independence images (Cloude, 1996) from the image taken on May 26, 2009. Figs. 8(a) and 8(b) indicate that the low entropy surface scattering above the large sandbank may have been caused by wind-wave-current interactions when the recorded wind speed was 7.9 m/s. In shallow waters, surface current varies depending on the actual water depth. Compared with the bathymetry data obtained in 2003, a displacement of 1.5 km on the small sandbank can be observed, and the elevation of the sandbank on March 15, 2009 was lower than that observed in 2003.

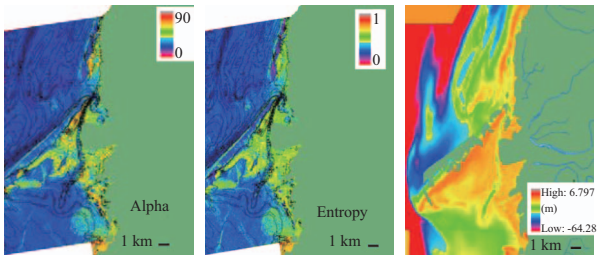


**Fig. 8. (a) Alpha of May 26, 2009; (b) entropy of May 26, 2009; and (c) bottom topography measured in 2003.**

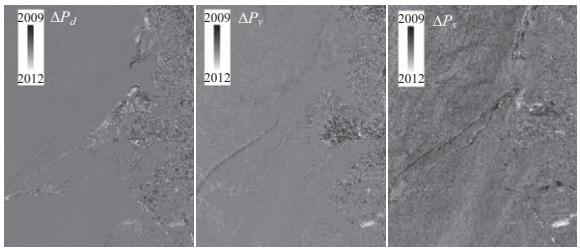


**Fig. 9. Difference in Y4R components on April 8 and May 3, 2012.**

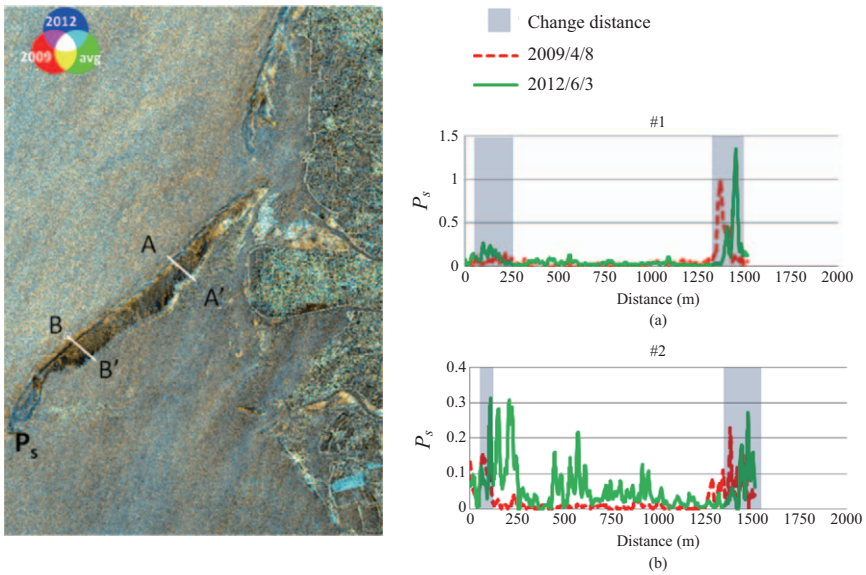


**Fig. 10. (a) 2009 and 2012 composite images; (b) sandbank displacement of A-A' profile; and (c) sandbank displacement of B-B' profile.**

## 4. Sandbank Displacement with the Same Tidal Levels

At the same tidal level, scattering mechanisms were expected to remain approximately the same if surface features were not changed by external forces. Two images, obtained on April 8, 2009 and June 3, 2012, were selected to perform a further quantitative analysis of sandbank displacement in this coastal region. The differences between the three decomposed components are shown in Fig. 9 for Y4R images. Strong double-bounce or weak volume scattering revealed the oyster farms, whereas $P_s$ indicated dynamic oceanic changes. The wind-wave interaction with the sandbank was also enhanced in $P_s$ component change; the features of the boundary of the sandbank in particular have significant displacements. In Fig. 10, composition with $P$ components in images from April 8, 2009 and June 3, 2012, the peak positions of the A-A' and B-B' profiles show that the sandbank is the A-A' profile of the eastern region, which shifted eastward by approximately 80 m; moreover, the B-B' profile of the west region moved approximately 90 m. These changes indicated counterclockwise displacement on the west coast, and a move further eastward on the eastern coast.

This phenomenon is supported by records obtained from

**Table 2. Average current recording at Mailiao Station from 1995 to 1996 (data from [Jan S. et al., 1997]).**

| Month | 1 | 2 | 3 | 4 | 5 | 6 | 7 | 8 | 9 | 10 | 11 | 12 |
|---|---|---|---|---|---|---|---|---|---|---|---|---|
| Current velocity (cm/s) | 14 | 17.2 | 5.1 | 2.6 | 3.6 | 5 | 7.9 | 4.9 | 3.3 | 9.6 | 11 | 17 |
| Current direction (deg) (going dir) | 180 | 177 | 154 | 105 | 87 | 47 | 46 | 53 | 139 | 173 | 168 | 181 |

**Table 3. Average current recordings at Budai Station in 2009 (data from Harbor and Marine Technology Center).**

| season | Winter | Spring | Summer | Autumn |
|---|---|---|---|---|
| Current velocity (cm/s) | 1.7 | 1.3 | 10.9 | 1.9 |
| Direction (going dir) | SE | SE | NNW | SSE |

Mailiao and Budai stations, presented in Tables 2 and 3, respectively. After the Yunlin industrial park and Mailiao Port projects were completed, the local current directions were reported to have been diverted by the breakwater embankment of Mailiao Port at the ebbing of the tide from the south to a west-southwest direction (Hsu et al., 2003). According to Jen et al. (1997), during the 6 -month "winter" period, the variation of current velocities is high and southward from October to the following March, with the most prevailing current direction being southward in offshore regions. During summer near Budai station, a current velocity of approximately 10.9 cm/s has been recorded, with strong currents coming from the north along this coastal region. This region has experienced a current velocity of approximately 15 cm/s during the winter monsoon season. These changes clearly indicate the environmental impact of inshore small- and medium-sized sandbanks. However, the tail of the large sandbank has moved toward land. The dislocation of this sandbank has also been suggested as being mostly due to seasonal strong current interactions.

## CONCLUSION

In this study, applications of polarization SAR images using RADARSAT-2 were analyzed. Different scattering mechanisms could be observed for oyster farms and sandbanks at different tidal levels. With Pauli-based and Y4R decompositions, oyster farms and sandbank regions could be identified. Additionally, the displacement of sandbanks could be analyzed using multitemporal SAR images. Pauli-based decompositions exhibit surface, double-bounce, and volume scattering, and the Y4R component could enhance such features with a $T$ matrix. From the target decomposition image of Pauli-based and Y4R approaches, double-bounce scattering is a favorable indicator for the presence of oyster farms, and surface scattering can delineate the water boundary of sandbanks, which can then be used to estimate a sandbank elevation model with the tidal level. At a C-band wavelength, scattering behavior is more sensitive to the ocean surface as it is wind-wave interaction and can result in increased multiple scattering and depolarization effects. In the offshore environment of Taiwan's west coast, strong double-bounce scattering and weak volume scattering were observed because of the characteristics of the oyster farm frame (densely arranged or rugged). The surface scattering components could identify sandbank changes under low and equal tidal-level conditions, which typically assume that sandbanks emerge on the surface or underwater because of the ebb and flow of the tide. Under low tide conditions, combining the low entropy of the surface scattering component and 2003 bottom topography between an offshore sandbank and inshore middle sandbank revealed a displacement of approximately 1.5 km under a tidal level of -1.14 m. Therefore, repeatedly acquired SAR images can be relied on for tidal-level data to estimate shallow sandbank topography. Furthermore, under the same tidal level, temporal changes in Pauli-based and Y4R images, namely in double-bounce or volume scattering, can reveal oyster farm areas, and the $P_s$ can indicate dynamic oceanic changes. Coastal sandbanks are enhanced in component changes in $P_s$. The results indicate counterclockwise displacement of sandbanks on Taiwan's west coast, and a move eastward on the eastern coast. The complex environment was probably influenced by ocean currents. The environmental effects of tide-current velocity from north to south (from the northern region) were more significant than from the south to north (from the southern region) along the coast, which in turn affected sandbank displacement.

## REFERENCES

Apel. J. R. (2004). Synthetic Aperture Radar Marine User's Manual; NOAA: Washington, DC, USA.

Brown I., S. Mwansasu and L. O. Weterberg (2016). L-Band Polarimetric Target Decomposition of Mangroves of the Rufiji Delta Tanzania. Remote Sensing 8(2), 140, doi: 10.3390/rs8020140.

Calkoen C. J., G. H. F. M. Hesselmans and G. J. Wensink (1998). The use of radar imagery to assess the bottom topography of shallow seas. International Hydrographic Review, LXXV(2).

Choe, B. H., D. J. Kim, J. H. Hwang, Y. Oh and W. M. Moon (2012). Detection of oyster habitat in tidal flats using multi-frequncy polarimetric SAR data. Estuarine, coastal and Shelf Science 97, 28-37.

Cloude S. R. and E. Pottier (1996). A review of target decomposition theorems in radar polarimetry. IEEE Transactions on Geoscience and Remote Sensing 34(2), 498-518.

Cloude S. R. and E. Pottier (1997). An entropy based classification scheme for land applications of polarimetric SAR. IEEE Transactions on Geoscience and Remote Sensing 35(1), 68-78.

Freeman A. and S. L. Durden (1998). A three-component scattering model for polarimetric SAR data. IEEE Transactions on Geoscience Remote Sensing 36(3), 963-973.

Freeman. A., Y. Shen and C. L. Werner (1990). Polarimetric SAR calibration experiment using active radar calibrators. IEEE Transactions on Geoscience Remote Sensing 28(2), 224-240.

Gade M., W. Alpers, C. Melsheimer and G. Tanck (2008). Classification of sediments on exposed tidal flats in the German Bight using multi-frequency radar data. Remote Sensing of Environment 112(4), 1603-1613.

Gao G., S. Gao, J. He and G. Li (2018). Ship detection using compact Polarimetric SAR based on the Notch filter. IEEE Transactions on Geoscience and Remote Sensing 99, 1-4

Gao G., S. Gao, J. He and G. Li (2018). Adaptive ship detection in Hybrid-Polarimetric SAR images based on the power-entropy decomposition. IEEE Transactions on Geoscience and Remote Sensing 99, 1-4

Harbor and Marine Technology center, Taiwan (2010). Oceanographical observation data-annual report 2009 (Current) 1, 5-8-1, 5-8-17.

Hong S. H. and S. Wdowinski (2012). Double-Bounce component in cross-polarimetric SAR from a new scattering target decomposition. IEEE Transactions on Geocience and Remote Sensing 52(6), 3039-3051

Hsu M. H., J. L. Yu and C. W. Cheng (2003). Measurements of ccean current in the vicinity of Yunlin offshore industrial estate. Proceedings of the 25th Ocean Engineering Conference in Taiwan, 579-586.

Huynen, J. R. (1970). Phenomenological theory of radar targets. Ph.D. dissertation, Univ. Technol, Delft, The Netherlands.

Industrial Development Bureau, Taiwan (2006). Field Investigation and Numerical Analysis for the Integrated Reclamation of Industrial District on Outer-bank of Yunlin PartII, No.1: Calibration and application of hydraulic and water quality dynamics in the near-and far-field ocean of the Industrial Area, 9-1-9-35

Jan S., J. Wang, C. S. Chern and S. Y. Chao (2002). Seasonal variation of the circulation in the Taiwan Strait. Journal of Marine Systems 35(3), 249-268.

Kim D. J., W. M. Moon, S. E. Park, J. E. Kim and H. S. Lee (2007). Dependence of waterline mapping on radar frequency used for SAR images in intertidal areas. IEEE geoscience and remote sensing letters 4(2), 269-273.

Kim T. H., C. S. Yang and K. Ouchi (2016). Interpretation of SAR image modulation by the interaction of current and bottom topography in Gyeonggi Bay with microwave scattering models. Journal of Marine Science and Technology 24(6), 1171-1180

Kim Y., D. H. Jang, N. W. Park and H. Y. Yoo (2016). Assessment of landform changes in Baramarae tidal flat, Korea using combined analysis of multi-temporal remote sensing images and grain size measurement data. Journal of Marine Science and Technology 24(6), 1070-1080.

Lee J. S. and E. Pottier (2009). Polarimetric radar imaging from basics to applications, CRC Press.

Lee, J. S., D. L. Schuler and T. L. Ainsworth (2000). Polarimetric SAR data compensation for terrain azimuth slope variation. IEEE Transactions on geoscience and remote sensing 38(5), 2153-2163.

Lee J. S., D. L. Schuler, T. L. Ainsworth, E. Krogager, D. Kasilingam and W.-M. Boerner (2002). On the estimation of polarization orientation shifts induced by terrain slopes. IEEE Transactions on Geoscience Remote Sensing 40(1), 30-41.

Lee J. S., K. P. Papathanassious, I. Hajnse, T. Mette, M. R. Grunes, T. Ainsworth and L. Ferro-Famil (2005). Applying polarimetric SAR interferometric data for forest classification. Geoscience and remote sensing symposium.

Lee J. S., M. R. Grunes, T. Ainsworth, I. Hajnsek, T. Mette and K. P. Papathanassious (2005). Forest classification based on L-Band polarimetric and Interferometric SAR data. Proceedings of the 2nd International workshop PolInSAR.

Lee J. S. and T. L. Ainsworth (2011). The Effect of Orientation Angle Compensation on Coherency Matrix and Polarimetric Target Decompositions. IEEE Transactions on Geoscience Remote Sensing 49(1), 53-64.

Lee, S. K., S. H. Hong, S. W. Kim and Y. Yamaguchi (2006). Polarimetric features of oyster farm observed by AIRSAR and JERS-1. IEEE Transactions on Geoscience Remote Sensing 44(10), 2728-2735.

Moon W. M., G. Staples, D. J. Kim, S. E. Park and K. A. Park (2010). Radarsat-2 and coastal applications: surface wind, waterline, and intertidal flat roughness. Proceedings of the IEEE 98, 800-815.

Niedermeier A., D. Hoja and S. Lehner (2005). Topography and morphodynamics in the German Bight using SAR and optical remote sensing data. Ocean Dynamics 55, 100-109.

Park S. E., W. M. Moon and D. J. Kim (2009). Estimation of Surface roughness parameter in intertidal mudflat using airborne polarimetric SAR data. IEEE Transactions on geoscience and remote sensing 47(4), 1022-1031.

Park S. E., W. M. Moon and E. Pottier (2012). Assessment of scattering mechanism of Polarimetric SAR signal from mountainous forest areas. IEEE Transactions on Geoscience and Remote Sensing 50, 4711-4719.

Ryu J. H., J. K. Choi and Y. K. Lee (2014). Potential of remote sensing in management of tidal flats: a case study of thematic mapping in the Korean tidal flats. Ocean and Coastal Management 102, 458-470.

Shuchman R. A., D. R. Lyzenga and G. A. Meadows (1985). Synthetic aperture radar imaging of ocean-bottom topography via tidal-current interactions: theory and observations. International Journal of Remote Sensing 6(7), 1179-1200.

Sun S., R. Liu and W. Wen (2015). Unsupervised classification method for polarimetric synethetic aperture radar imagery based on Yamaguchi four-component decomposition model. Journal of Electrical and Computer Engineering 2015, Article ID 680715, http://dx.doi.org/10.1155/2015/680715.

Tanck G., W. Alpers and M. Gade (1999). Determination of Surface Roughness Parameters of Tidal Flats from SIR-C/X-SAR 3-Frequency SAR Data. Geoscience and Remote Sensing Symposium.

Varghese A. O., A. Suryavanshi and A. K. Joshi (2016). Analysis of different polarimetric target decomposition methods in forest density classification using C band SAR data. International Journal of Remote Sensing 37(3), 694-709.

Wal D. v. d., P. M. J. Herman and A. W. v. d. Dool (2005). Characterisation of surface roughness and sediment texture of intertidal flats using ERS SAR imagery. Remote Sensing of Environment 98, 96-109.

Wang H. W, K. S. Chen, Z. L. Lin and Y. Liu (2016). Quantitative analysis of shoreline changes in west Taiwan coast using time-series SAR images 9(11), 4898-4907.

Water Resources Agency, Taiwan (2001). Establishment of Wave, Tidal Current and Coastal Evolution Models, 4-65-4-84.

Yamaguchi Y., T. Moriyama, M. Ishido and H. Yamada (2005). Four component scattering model for polarimetric SAR image decomposition. IEEE Transactions on Geoscience Remote Sensing 43(8), 1699-1706.

Yamaguchi Y., Yuki Yajima and Hiroyoshi Yamada (2006). A Four-Component Decomposition of POLSAR Images Based on the Coherency Matrix. IEEE Transactions on Geoscience Remote Sensing Letter 3(3), pp. 292-296.

Yamaguchi, Y., A. Sato, W. M. Boerner, R. Sato and H. Yamada (2011). Four-component scattering power decomposition with rotation of coherency matrix. IEEE Transactions on Geoscience Remote Sensing 49(6), 2251-2258.

Zhai W. and C. Huang (2016). Fast building damage mapping using a single post-earthquake PolSAR image: a case study of the 2010 Yushu eqrthquake. Earth, Planets and Space 68(86), doi:10.1186/s440623-016-469-2.

Zhang S., Q. Xu, Q. Zheng and X. Li (2017). Mechanisms of SAR Imaging of shallow water topography of the Subei Bank. Remote Sensing 9(11), 1203, doi:10.3390/rs9111203.